PERGAMON

International Journal of Heat and Mass Transfer 43 (2000) 4347–4359

International Journal of HEAT and MASS TRANSFER

www.elsevier.com/locate/ijhmt

Three-dimensional numerical simulation of rotating spoke pattern in an oxide melt under a magnetic field

C.J. Jing[a], N. Imaishi[a,*], S. Yasuhiro[a], T. Sato[a], Y. Miyazawa[b]

[a]*Institute of Advanced Material Study, Kyushu University, 6-1 Kasuga-koen, Kasuga, Fukuoka 816-8580, Japan*
[b]*National Institute for Research in Inorganic Materials, 1-1 Namiki, Tsukuba, Ibaraki 305-0044, Japan*

Received 23 July 1999; received in revised form 12 November 1999

Abstract

On the surface of various oxide melts under a vertical magnetic field, the rotating spoke pattern appears. In order to provide a first basic view of this phenomenon, a series of three-dimensional numerical simulations of $LiNbO_3$ melt flow in a crucible ($47\ mm^{\phi} \times 46\ mm^{H}$) under a uniform vertical magnetic field were performed. In this model, the oxide melt was assumed to be a dielectric fluid with a uniform electric charge density c_e^0. The Marangoni effect was also taken into account. The simulations indicated that the spoke pattern is caused by the Marangoni instability and the rotating motion is driven by the Lorentz force caused by the interaction between the vertical magnetic field and the radial motion of charged fluid which is driven by the Rayleigh–Marangoni convection in the crucible. A charge density of 0.1 C/m^3 is sufficient to express the experimentally observed rotating spoke patterns on the $LiNbO_3$ melt which were reported by Miyazawa et al. (1996).

Keywords: Numerical simulation; Rotating spoke pattern; Magnetic field; Marangoni effect

1. Introduction

Many authors have reported on the so-called spoke pattern on oxide melts during single crystal growth in the Czochralski system [1–9]. The spoke patterns were numerically reproduced in our previous report [10] by using a three-dimensional unsteady numerical code which took the Marangoni effect into account. These simulations clarified that the Marangoni instability in the thermal boundary layer beneath the melt surface causes temperature and velocity disturbances in the azimuthal direction. The dark spoke lines correspond to the lower temperature zone to which the surface flow converges. Besides these spoke patterns, since 1993, Miyazawa and co-workers have been demonstrating experimentally that the spoke pattern exhibits azimuthal rotating action under a vertical magnetic field. The rotating spoke pattern has been observed in many, but not all, oxide melts, such as TiO_2, Nd_3Ga5O_{12}, $NdGaO_3$, $Gd_3Ga_5O_{12}$, $YAlO_3$, $LiNbO_3$, $BiSiO_{20}$ and β-BBO [11–18]. However, there exists no theoretical explanation for the onset of the rotating spoke pattern, so far. The azimuthal rotation must be caused by some kind of thermoelectric effect. The most plausible cause is the Lorentz force, which is created by an interaction between the vertical magnetic field and electric current in the melt. Oxide melts exhibit electric conductivity [5] since they are partially dissociated and exhibit ionic, but not electronic, conduc-

* Corresponding author. Tel.: +81-92-583-7793; fax: +81-92-583-7796.
E-mail address: imaishi@cm.kyushu-u.ac.jp (N. Imaishi).

0017-9310/00/$ - see front matter
PII: S0017-9310(00)00053-3

Nomenclature

$\boldsymbol{b}$	magnetic field intensity
b_0	characteristic magnetic field intensity
c_e	charge density
c_e^0	characteristic charge density
$\boldsymbol{e}$	electric field intensity
$\boldsymbol{e}_z$	z-directional unit vector
g	acceleration due to gravity
Gr	Grashof number, $Gr = g\beta T_m r_c^3/\nu^2$
h	crucible height
$\boldsymbol{j}$	electric current density
Ma	Marangoni number, $Ma = \gamma_T \Delta T \delta/(\mu\alpha)$
M_d	magnetic Reynolds number, $M_d = c_e^0 b_0 r_c^2/(\rho\nu)$
P	pressure
Pr	Prandtl number
q	heat flux of crucible side wall
r_c	radius of crucible
Re_γ	capillary Reynolds number, $Re_\gamma = \gamma_T T_m r_c/(\mu\nu)$
R_{ad}	radiation number, $R_{ad} = \sigma\varepsilon T_m^3 r_c/\lambda$
T	dimensional temperature
T_m	melting point
t	time
$\boldsymbol{v}$	fluid velocity

Greek symbols

α	thermal diffusivity
β	thermal expansion coefficient of melt
ε	emissivity
γ_T	temperature coefficient of surface tension, $-\partial\gamma/\partial T$
λ	thermal conductivity
μ	viscosity
τ	nondimensional time
ν	kinematic viscosity
Θ	nondimensional temperature
Θ_a	nondimensional effective ambient temperature
Θ_m	nondimensional melting point
ρ	density
σ	Stefan–Boltzmann constant
σ_e	electric conductivity

Subscripts

r, θ, z	cylindrical coordinates

tivity [19]. The motions of ions interact with the vertical magnetic field to produce the Lorentz force. The rotating spoke patterns could be simulated if the convective diffusion equations of anions and cations were analyzed in combination with the energy equation and the Navier–Stokes equation with the Lorentz force terms under a vertical magnetic field as shown in Appendix A. Unfortunately, the lack of knowledge regarding physicochemical properties of oxide melts prevents us from solving these equations, Eqs. (A4)–(A10). In order to begin quantitative discussion on the phenomenon, a numerical simulation based on a very simple model is of significance as a first approximation. Because the spoke pattern is a three-dimensional (3D) unsteady phenomenon, the simulation has to be conducted with a 3D unsteady numerical code. This paper presents a series of 3D numerical simulations of the rotating spoke pattern on the $LiNbO_3$ melt in an open crucible using a very crude model.

2. Formulation of the problem

2.1. Basic assumptions and governing equations

By taking into account the effect of constant magnetic fields on hydrodynamic processes, and the heat and mass transport in semiconductor melts and liquid metals, it is customary to use the magnetohydrodynamics (MHD) approximation [20]. The MHD approximation often assumes electronic conductivity and neglects the effect of the charged particles [21–23]. Thermoelectromagnetic convection (TEMC), which takes into account the thermo-electromotive force and thermocurrent (the Seebeck effect), can explain the azimuthal motion of semiconductor melts and liquid metals in a magnetic field [24,25]. The Seebeck effect occurs in materials with free electrons. Thus, the analysis based on the conventional MHD and TEMC treatments does not seem applicable to oxide melt cases because the oxide melts are basically dielectrics but are partially dissociated and exhibit rather poor ionic electrical conductivity [5]. However, the Lorentz force is a potential candidate for the force that propels the melt in the azimuthal direction. The authors believe that the interaction between the vertical magnetic field and the dissociated charged particles, that is, anions and cations, creates the force.

The dissociated melt satisfies the neutrality condition at all points, otherwise there appears an electric field. The rigorous analysis of ion transport, as described in Appendix A, provides information on the differences in the migration rates of anions and cations and

tempo-spatio disturbances of electric charge accompanied by a local electric field. These apparent net charges may interact with the applied vertical magnetic field to create the Lorentz force locally and temporally in the oxide melt.

Unfortunately, very limited information is available on the physicochemical properties of oxide melts, such as electrical conductivity [5] and the dissociation equilibrium [19] of $LiNbO_3$. The lack of knowledge regarding fundamental properties, such as diffusivity and mobility of ions, prevents us from analyzing the whole set of fundamental equations, Eqs. (A4)–(A10), for the rotating spoke pattern. As a first approximation, we introduced the following crude assumptions for the electric properties of oxide melts.

According to the electromagnetic field theory, the electric current $\boldsymbol{j}$ in any substance can be generally expressed as $\boldsymbol{j} = c_e\boldsymbol{v} + \sigma_e(\boldsymbol{e} + \boldsymbol{v} \times \boldsymbol{b})$. Oxide melts have such small electrical conductivity that we assume that (i) the induced current density (the second term) is negligible and the convective electric current (the first term) should be retained, because there is no available data on the charge density c_e, (ii) oxide melts have an apparent positive charge with a uniform charge density c_e^0. These assumptions are introduced as a first-approximation model without any justification. The apparent positive charge could correspond to such a case as the mobility of the positive ion is larger than that of the negative ion.

We consider the oxide melt flow under a steady uniform vertical magnetic field, $\boldsymbol{b} = b_0\boldsymbol{e}_z$, in a crucible of radius r_c and height h, as illustrated in Fig. 1. Our model also involves the following basic hydrodynamic assumptions: (iii) the melt is an incompressible Newtonian fluid satisfying the Boussinessq approximation except for the surface tension, (iv) the flow is laminar, (v) the viscous dissipation is negligible, (vi) the free surface is planar and nondeformable and (vii) the melt is opaque.

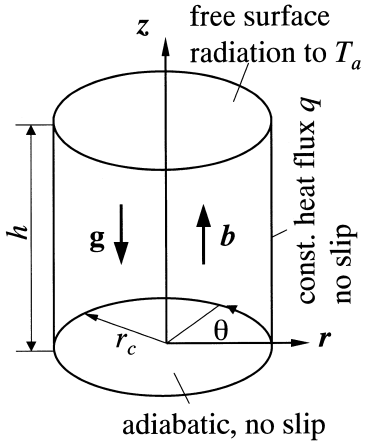

Fig. 1. The schematic of the system.

The boundary conditions are set as follows. At the free surface, the Marangoni effect is considered, and for the other boundaries the no-slip condition is used. According to the global thermal analysis [26,27], the bottom of the crucible is set to be adiabatic and the crucible side wall is assumed to be heated with a constant heat flux q. The heat loss from the free surface is caused by radiation to the ambient of effective temperature T_a.

Thus, the fundamental equations can be expressed in nondimensional form as

$$\nabla \cdot \boldsymbol{V} = 0, \tag{1}$$

$$\frac{\partial \boldsymbol{V}}{\partial \tau} + \boldsymbol{V} \cdot \nabla \boldsymbol{V} = -\nabla P + \nabla^2 \boldsymbol{V} + \mathrm{Gr}(\Theta - \Theta_m)\boldsymbol{e}_Z + M_d(\boldsymbol{J} \times \boldsymbol{B}), \tag{2}$$

$$\frac{\partial \Theta}{\partial \tau} + \boldsymbol{V} \cdot \nabla \Theta = \frac{1}{Pr}\nabla^2 \Theta, \tag{3}$$

$$\boldsymbol{J} = C_e \boldsymbol{V}, \tag{4}$$

and the boundary conditions can be expressed as

at the surface ($z = h$, $0 \le r < r_c$, $0 \le \theta < 2\pi$)

$$\frac{\partial V_r}{\partial Z} = Re_\gamma \frac{\partial \Theta}{\partial R}, \quad \frac{\partial V_\theta}{\partial Z} = Re_\gamma \frac{\partial \Theta}{R\partial \theta}, \quad V_z = 0, \quad -\frac{\partial \Theta}{\partial Z} = R_{ad}(\Theta^4 - \Theta_a^4), \tag{5}$$

at the crucible wall ($0 < z \le h$, $r = r_c$, $0 \le \theta < 2\pi$)

$$V_r = V_\theta = V_z = 0, \quad \frac{\partial \Theta}{\partial R} = Q, \tag{6}$$

and at the bottom ($z = 0$, $0 < r < r_c$, $0 \le \theta < 2\pi$)

$$V_r = V_\theta = V_z = \frac{\partial \Theta}{\partial Z} = 0. \tag{7}$$

The dimensionless parameters are defined as

$$\text{Grashof number:} \qquad Gr = \frac{g\beta T_m r_c^3}{\nu^2} \tag{8}$$

Magnetic Reynolds number: $$M_d = \frac{c_e^0 b_0 r_c^2}{\rho\nu} \quad (9)$$

Capillary Reynolds number: $$Re_\gamma = \frac{\gamma_T T_m r_c}{\mu\nu} \quad (10)$$

Prandtl number: $$Pr = \frac{\nu}{\alpha} \quad (11)$$

Radiation number: $$R_{ad} = \frac{\sigma\varepsilon T_m^3 r_c}{\lambda} \quad (12)$$

The following nondimensionalization was used.

$$\begin{aligned} &(R, Z, H) = \frac{(r, z, h)}{r_c}, \\ &(V_r, V_z, V_\theta) = \frac{(v_r, v_z, v_\theta) r_c}{\nu}, \quad P = \frac{p r_c^2}{\rho\nu^2}, \\ &(\Theta, \Theta_a) = \frac{(T, T_a)}{T_m}, \quad \tau = \frac{t\nu}{r_c^2}, \quad Q = \frac{q r_c}{\lambda T_m}, \\ &\boldsymbol{J} = \frac{\boldsymbol{j} r_c}{c_e^0}, \quad \boldsymbol{B} = \frac{\boldsymbol{b}}{b_0}, \quad C_e = \frac{c_e}{c_e^0}. \end{aligned} \quad (13)$$

2.2. Numerical method and calculation conditions

The fundamental equations were solved by the finite-difference method with the HS-MAC algorithm on a $40^r \times 40^z \times 60^\theta$ nonuniform grid. The details are described elsewhere [10].

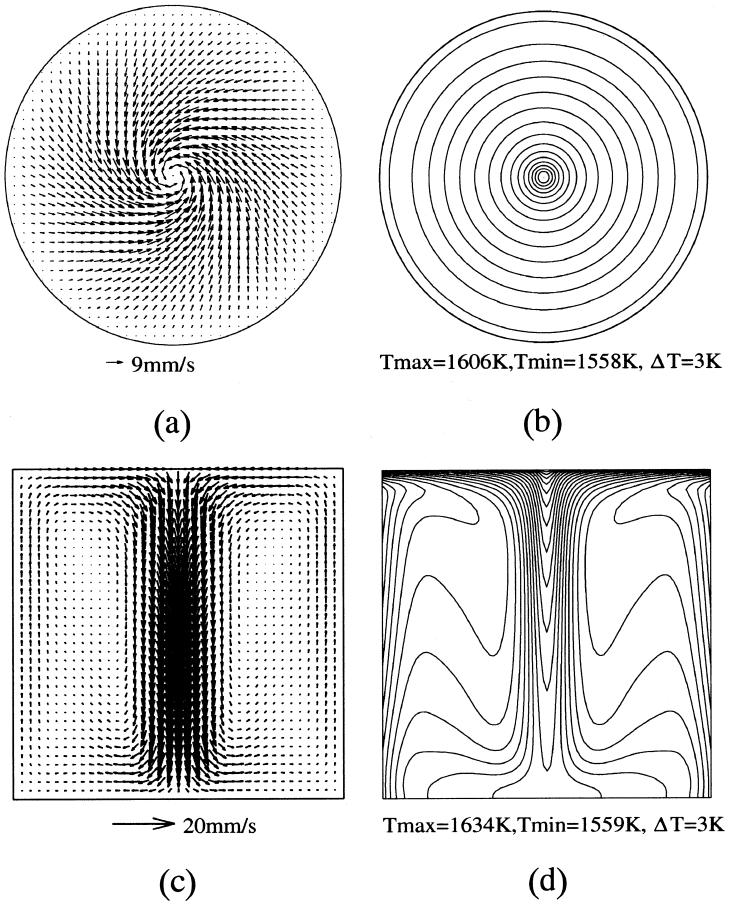

Fig. 2. The top views (a, b) and meridional views (c, d) of velocity vectors and isotherms of the axisymmetric, steady-state solution with $Re_\gamma = 0$. The isotherms are drawn at every $\Delta T = 3$ K. The other nondimensional parameters are $M_d = 10^{-3}$, $Gr = 2.62 \times 10^5$, $Pr = 13.6$, $R_{ad} = 0.34$, $Q = 0.07$ and $\Theta_a = 0.8$.

The following simulations will be compared with the experimental report of Miyazawa et al. [16,28] on $LiNbO_3$ melt flow. The radius of the crucible is $r_c = 23.5$ mm and the height $h = 46$ mm. The thermophysical properties of the $LiNbO_3$ melt at 1573 K are taken from [6] and listed in [10]. Then the dimensionless numbers are $Gr = 2.62 \times 10^5$, $Re_\gamma = 2.32 \times 10^4$, $Pr = 13.6$ and $R_{ad} = 0.34$. The heat flux Q in Eq. (6) was estimated to be $Q = 0.07$ by applying the global analysis code [27] to the experimental condition of Miyazawa et al. [16,28]. The code also suggests that the heat flux at the bottom of the crucible is small enough to satisfy the boundary condition given in Eq. (7). The effective ambient temperature is set to be $\Theta_a = 0.8$ in order to match the calculated temperature at the bottom of the crucible with Miyazawa and coworkers' measured value, that is, about 100 K above the melting point. The results based on this set of parameters are presented below.

3. Results and discussion

3.1. The significance of the Marangoni effect

Fig. 2 shows the 3D flow and temperature fields without the Marangoni effect under a vertical magnetic field ($M_d = 10^{-3}$). The flow is steady and axisymmetric. However, when the Marangoni effect is taken into account, the solution exhibits a time-dependent 3D structure. Illustrations of the velocity vectors and isotherms on the surface are shown in Fig. 3. The convergent flow (Fig. 3a) and the surface temperature field (Fig. 3b and c) obtained by the calculation look similar

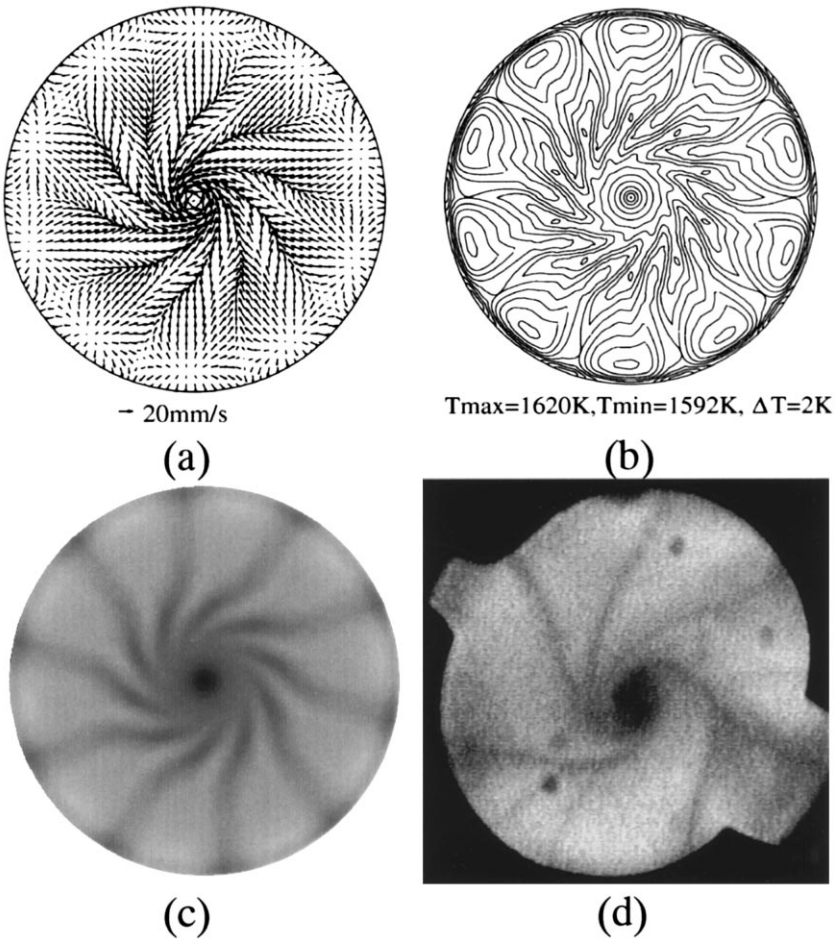

Fig. 3. The illustration of the numerically simulated surface pattern and an experimetal picture of surface pattern of the $LiNbO_3$ melt. (a) the surface velocity vectors, (b) the evenly spaced surface isotherms at every 2 K, (c) the visualized gray-scale surface temperature field, (d) the experimentally observed surface spoke pattern under $b_0 = 1$ T. The calculation conditions are $M_d = 10^{-3}$, $Gr = 2.62 \times 10^5$, $Re_\gamma = 2.32 \times 10^4$, $Pr = 13.6$, $R_{ad} = 0.34$, $Q = 0.07$, $\Theta_a = 0.8$.

to the experimental pattern (Fig. 3d) obtained under the same thermal conditions and $b_0 = 1$ T [16,28]. Calculated result indicates that the surface pattern is rotating and the angular velocity is about 0.03 rad/s. The velocity and temperature distributions in several cross-sections are shown in Fig. 4. As shown in Fig. 4a, d and g, the rotation is counter-clockwise in the upper-half region and clockwise in the lower half. The azimuthal velocity near the surface is much faster than that in the lower-half region. Fig. 4b, e and h show the isotherms and Fig. 4c, f and i show the contours of the axial velocity. The upward and downward flow are indicated by the solid lines and the dotted lines, respectively. Beneath the surface, 3D patterns are domi-

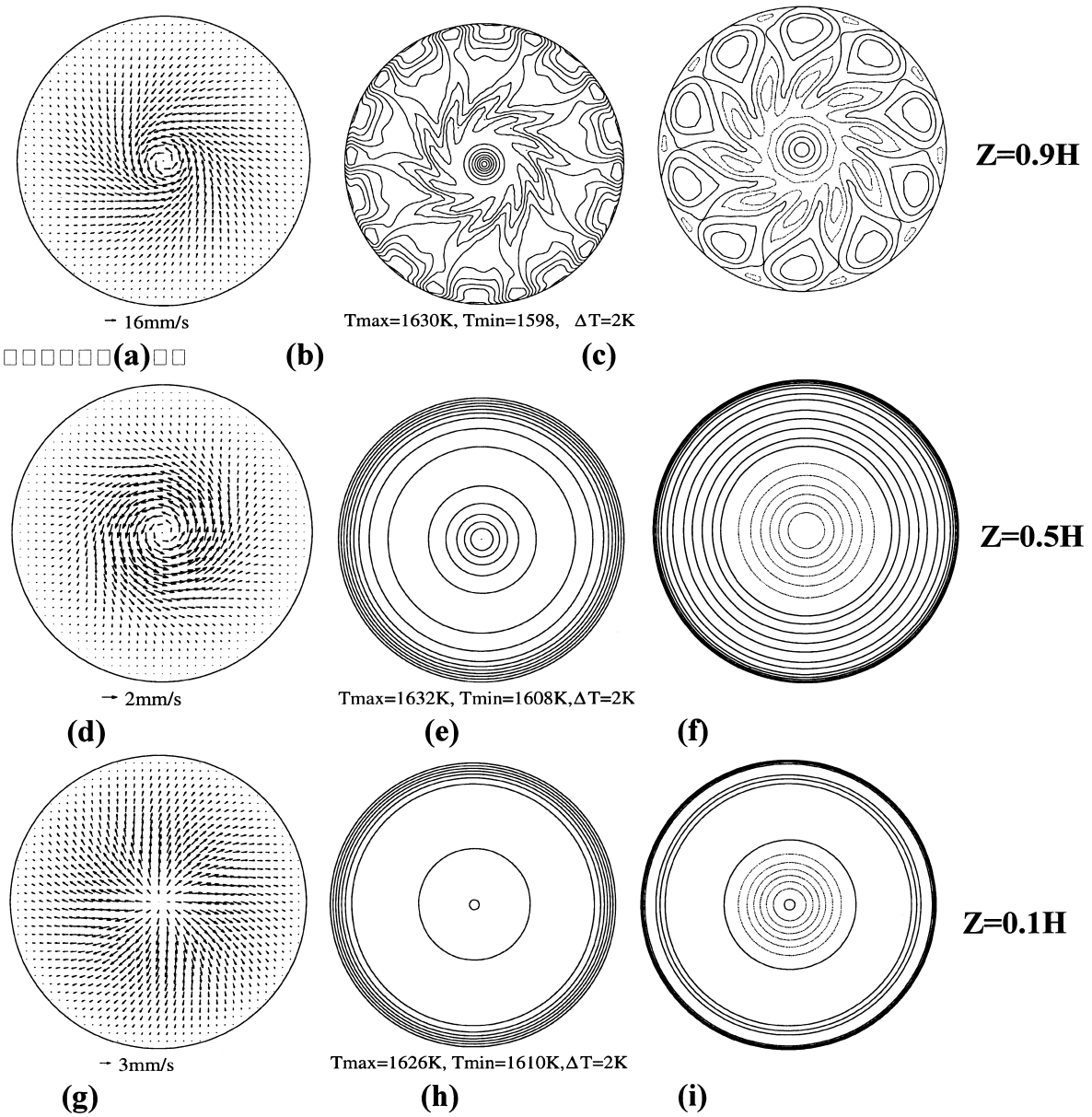

Fig. 4. The numerically simulated bulk flow and temperature fields. (a)–(i) illustrate the velocity vectors and isotherms every 2 K on three horizontal cross-sections, (j, k) the meridional views of $\theta = 0$ and (l, m) the circumferential views at $R = 0.8$. The nondimensional parameters are identical to those shown in Fig. 3.

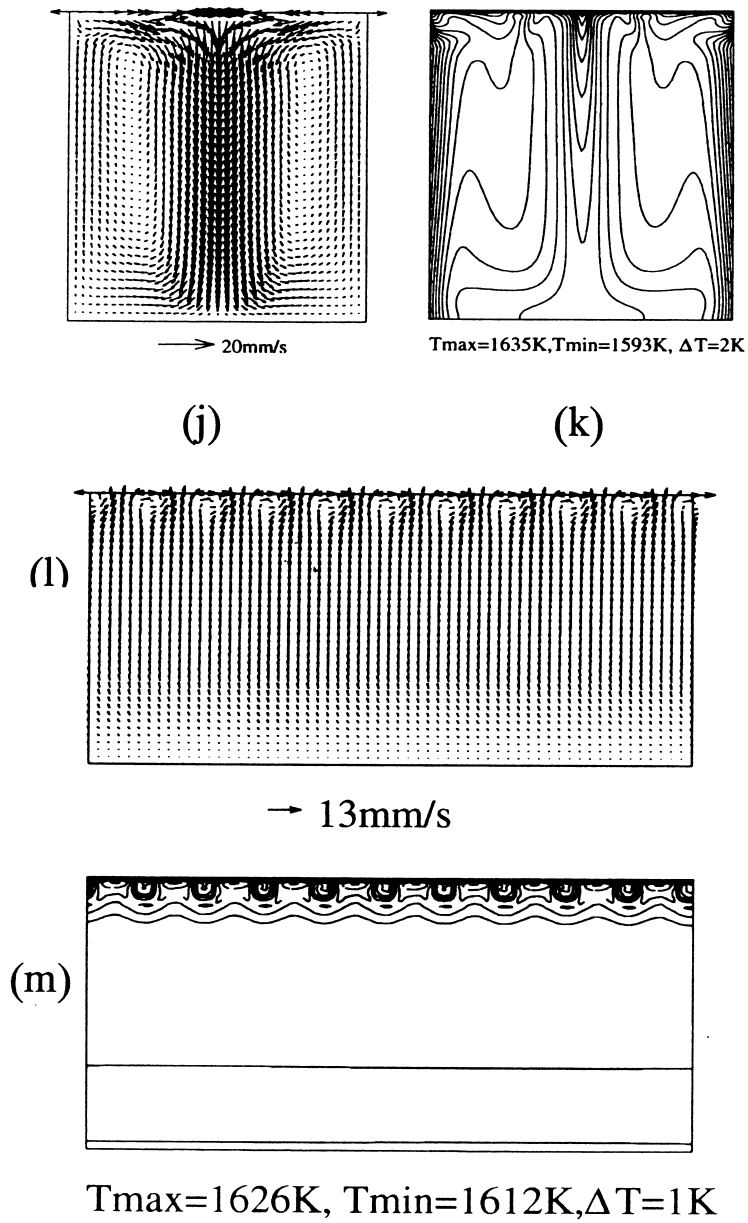

Fig. 4 (*continued*)

nant. These 3D structures disappear approximately 7 mm below the surface and the temperature field and the contours of the axial velocity become monotonically axisymmetric in the lower-half region. Fig. 4j–m show the meridional and circumferential views of the velocity and temperature fields. Similar to the spoke patterns without a magnetic field [1,10], the rotating spoke pattern is also a localized phenomenon near the surface.

3.2. The effect of M_d

The nondimensional number M_d reflects the product of the magnetic field intensity b_0 and the electric charge density c_e^0. A series of calculations were conducted to determine the effect of M_d with $Gr = 2.62 \times 10^5$, $Re_\gamma = 2.32 \times 10^4$, $R_{ad} = 0.34$, $Q = 0.07$ and $\Theta_a = 0.8$. Fig. 5 shows the variation of the surface patterns with the increase of M_d. When M_d is less than

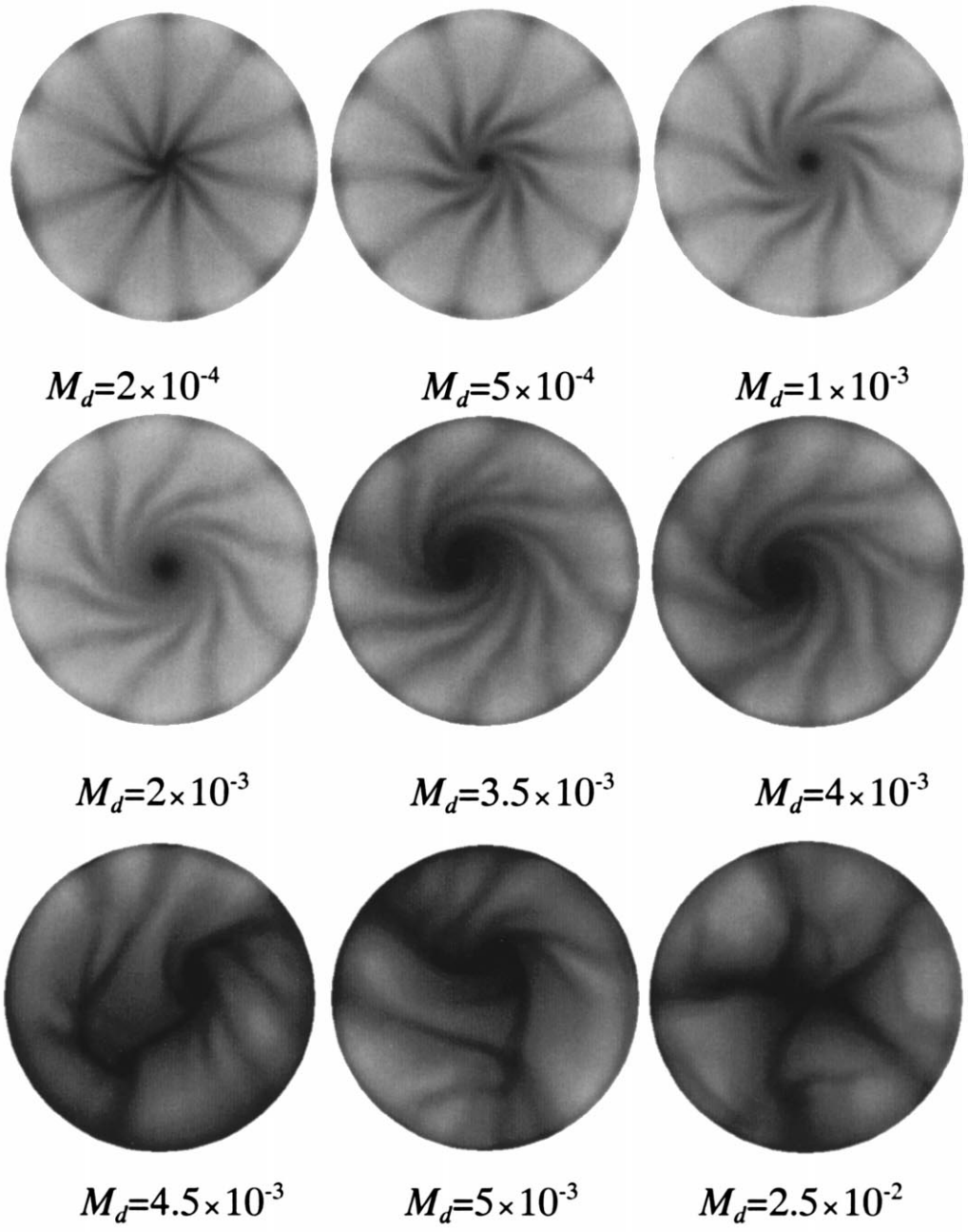

Fig. 5. Effect of M_d on the surface temperature and velocity distributions. The calculation conditions, except for M_d, are the same as those in Fig. 3. (A) Grey scale expressions of instantaneous surface temperature distribution under different M_d values. (B) Surface velocity distributions at the same instances as corresponding figure in (A).

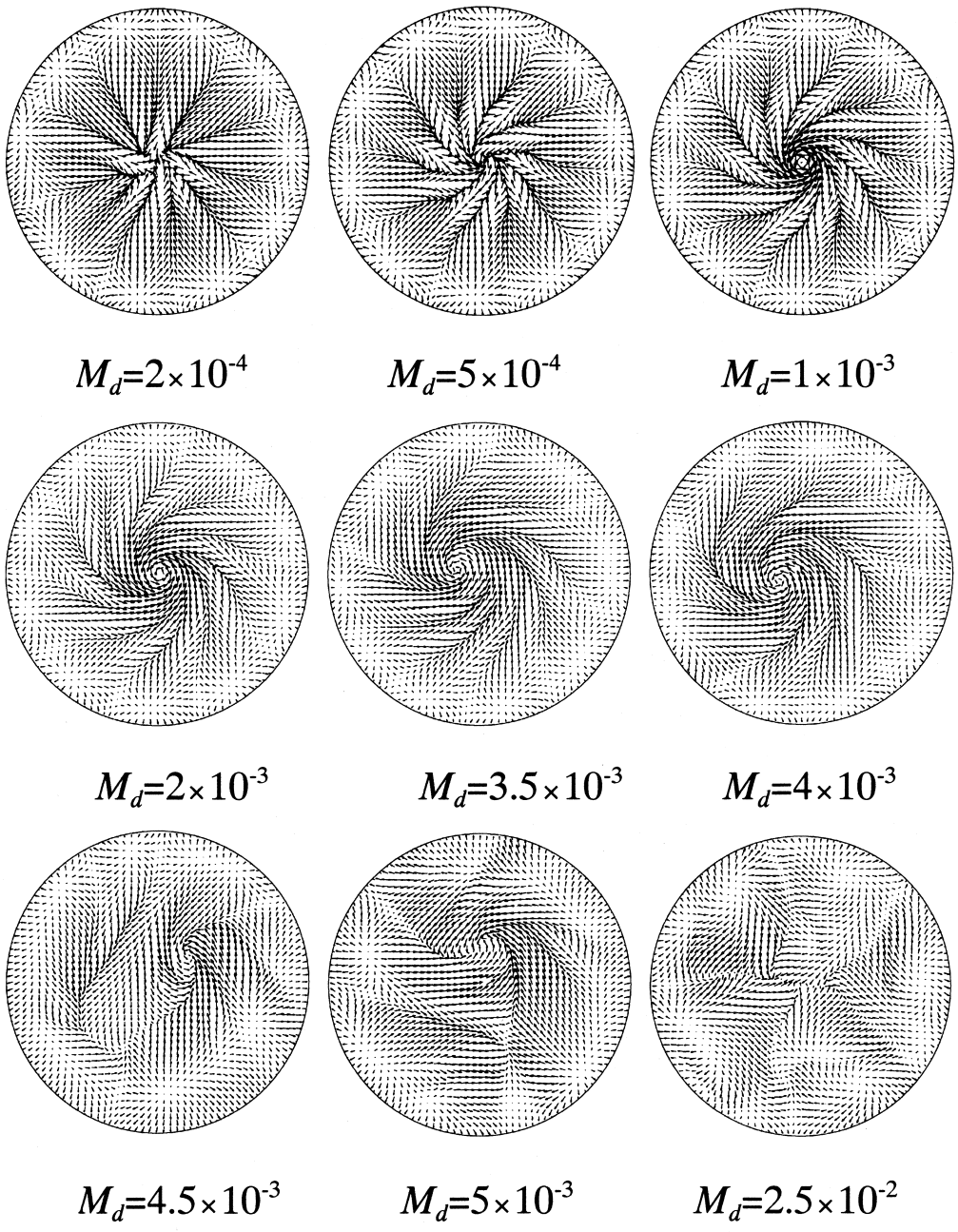

Fig. 5 (*continued*)

about 2×10^{-4}, the spoke lines on the melt surface maintain themselves straight. However, if M_d becomes greater than 2×10^{-4}, the spokes begin skewing near the center, and with an increase of M_d, the skewed portion extends toward the crucible wall. With $M_d = 2.5 \times 10^{-2}$, the simulation results do not predict rotating spoke patterns, but instead, predict a type of rotating-network pattern with many spontaneous hot spots, pop-up positions of which move successively in the azimuthal direction as shown in the last figure of Fig. 5A and B. This type of rotating pattern was also observed in the $LiNbO_3$ melt with a congruent composition at a high magnetic field [29]. The effects of M_d on the characteristics of the bulk flow and rotating spoke patterns are plotted in Fig. 6. With increasing M_d, significant increases of the maximum radial and azimuthal velocities and a decrease of the maximum axial velocity occur, as shown in Fig. 6a and b, shows the effect of M_d on the angular velocity of the surface patterns and the number of spokes. The evolution of the rotation occurs in the following manner. Once the vertical magnetic field is applied, the melt starts rotating and the rotation angular velocity increases with M_d in the range of $0 < M_d < 5 \times 10^{-3}$. The time evolution of the rotating spoke pattern at $M_d = 3.5 \times 10^{-3}$ is shown in Fig. 7. The calculated result gives $\omega = 0.24$ rad/s and the number of spokes $N = 10$, which is in agreement with the experimentally observed angular velocity of 0.8 rad/s and $N = 9$–10 at about $b_0 = 1.0$ T, see Fig. 3d. If $M_d = 3.5 \times 10^{-3}$ is assumed under a magnetic field intensity $b_0 = 1.0$ T, the charge density c_e^0 must be about 0.1 C/m^3 in order to correspond to the experimental condition for the $LiNbO_3$ melt, or [unit charge/2×10^{10} molecules]. The number of spokes is maintained almost constant if $M_d < 2 \times 10^{-3}$. With further increase of M_d, the number of skewed spokes (or the low temperature lines which separate hot spots) decreases. With $M_d > 5 \times 10^{-3}$, rotating network patterns becomes dominant. These trends are consistent with the experimental observations.

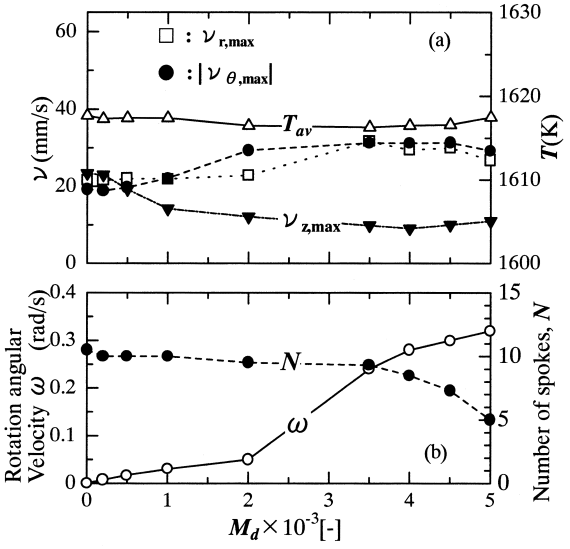

Fig. 6. The effect of M_d the characteristics values of the rotating melt flow.

Present model successfully explains the rotating spoke patterns on oxide melt surfaces experimentally observed under vertical magnetic field. This model, however, could not explain the experimental observation of the temperature increase at the crucible bottom, as reported by Miyazawa and Michino [28,29]. They recognized the crucible bottom temperature increases as a sign of the incipience of rotating motion in various oxide melts which do not exhibit the spoke pattern.

These disagreements could be attributed to the oversimplification employed in this model, such as the uniformly distributed constant charge density in the oxide melt. These will be resolved by solving the whole set of fundamental equations, Eqs. (A4)–(A10), provided adequate data on thermodynamic and thermophysical properties of the melt. Furthermore, we must give adequate consideration to the soluto-capillary effect which is accompanied by various type of redox reactions which occur on the melt surface under a reducing gas atmosphere, such as nitrogen + hydrogen. The details of these redox reactions are not yet well understood.

4. Conclusions

A series of 3D numerical simulations of the $LiNbO_3$ melt flow under a vertical magnetic field were performed based on a simplified mathematical model which assumes the melt to be a dielectric fluid with a uniform electric charge density. With this model, the azimuthal motion was propelled by the Lorentz force which acts in the azimuthal direction as a result of the interaction between the vertical magnetic field and the radial motion of the charged melt driven by the convection caused by the buoyancy and the thermocapillary effects in the crucible. The Rayleigh effect alone is insufficient to explain the spoke pattern. The Marangoni effect was essential to explain the appearance of the spoke pattern. This crude model could semiquantitatively explain the experimentally observed rotating spoke pattern, such as the number of spokes, the rotation rate, and their dependence on the magnetic field intensity.

In this study, an assumption of uniform charge density was employed without any discussion as to how the charge is brought about. More detailed physicochemical background is required to understand the

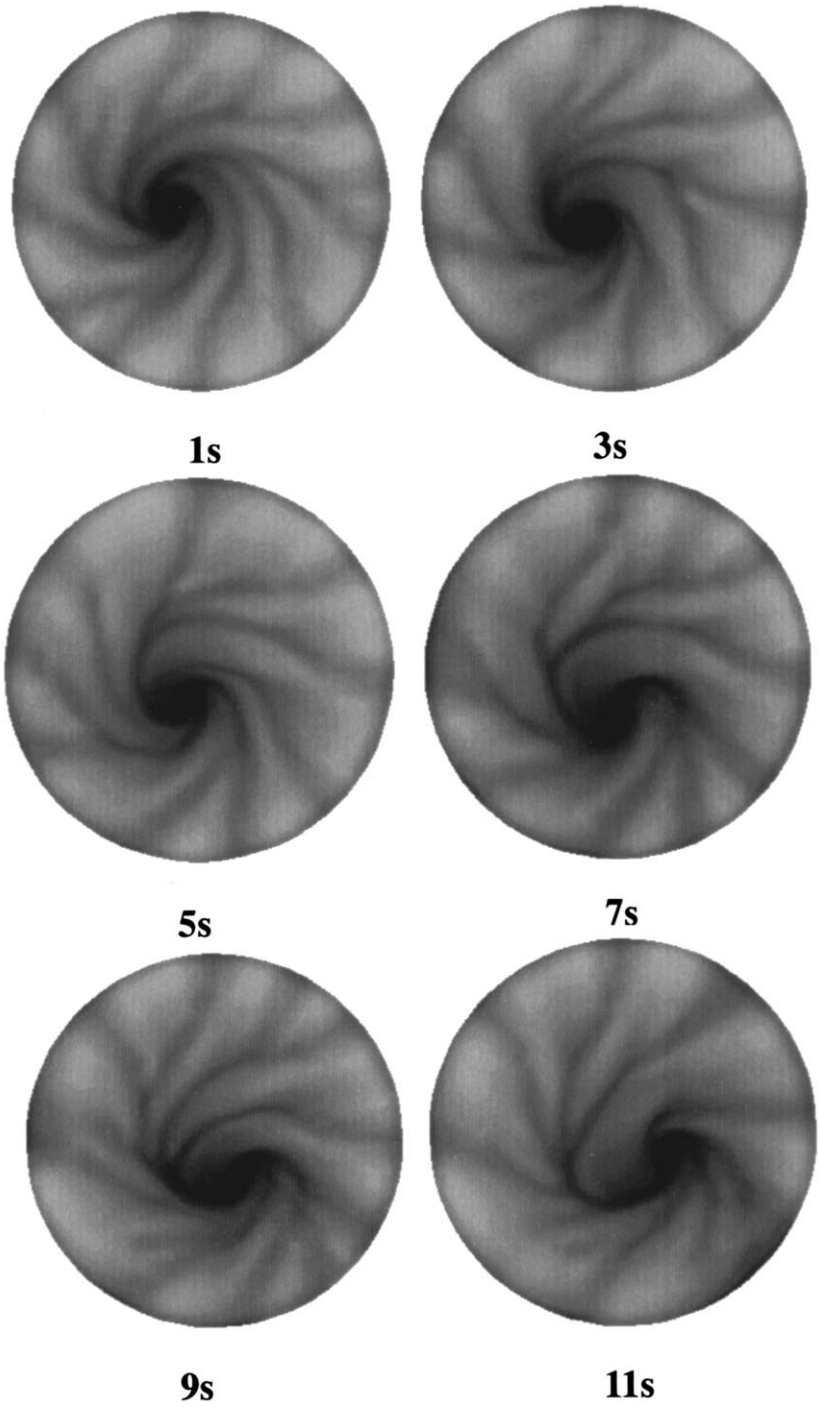

Fig. 7. Snap-shots of the calculated rotating spoke pattern (gray scale expression of instantaneous surface temperature distributions) at every 2 s. Condition: $M_d = 3.5 \times 10^{-3}$, $Gr = 2.62 \times 10^5$, $Re_\gamma = 2.32 \times 10^4$, $Pr = 13.6$, $R_{ad} = 0.34$, $Q = 0.07$ and $\Theta_a = 0.8$.

unique flow behavior of oxide melts under vertical magnetic field.

Acknowledgements

Part of the 3D numerical solver used in this work was developed in the "Technology for Production of High Quality Crystals" research program which is supported by the NEDO through the JSUP in the Program of MITI.

Appendix A

According to Uda and Tiller [19], in the $LiNbO_3$ melt the following dissociation equilibrium exists

$$2LiNbO_3 = Li_2O + Nb_2O_5 \tag{A1}$$

$$Li_2O = Li^+ + LiO^- \tag{A2}$$

$$Nb_2O_5 = Nb_2O_4^{2+} + O^{2-} \tag{A3}$$

For the dissociated $LiNbO_3$ melt, the flow under a magnetic field could be governed by the following equations

Continuity equation:
$$\nabla \cdot \mathbf{v} = 0 \tag{A4}$$

Momentum equation:

$$\rho \frac{D\boldsymbol{v}}{Dt} = -\nabla p + \mu \nabla^2 \boldsymbol{v} + \rho g\left[1 - \beta(T - T_m)\right] + \boldsymbol{j} \times \boldsymbol{b} \tag{A5}$$

Energy equation:
$$\frac{DT}{Dt} = \alpha \nabla^2 T \tag{A6}$$

Ohm's law:

$$\boldsymbol{j} = \sum_{i=1}^{2} z_i N q\left(c_i^+ - c_i^-\right)\boldsymbol{v} + \sigma_e(\boldsymbol{e} + \boldsymbol{v} \times \boldsymbol{b}) \tag{A7}$$

Charged species:

$$\frac{Dc_i^{\pm}}{Dt} = \pm \zeta_i^{\pm} c_i^{\pm} \nabla^2 \phi + D_i^{\pm} \nabla^2 c_i^{\pm} + \eta_i n_i - k_i c_i^+ c_i^- \tag{A8}$$

Neutral species:

$$\frac{Dn_i}{Dt} = D_i \nabla^2 n_i - g_i n_i + k_i c_i^+ c_i^- \tag{A9}$$

Electric Potential Equation:

$$\Delta^2 \phi = -\frac{\sum_{i=1}^{2} z_i N q\left(c_i^+ - c_i^-\right)}{\varepsilon} \tag{A10}$$

Here, ϕ is the electric potential, $\boldsymbol{e} = -\Delta\phi$ the electric field intensity, ε the permeability, c the charge mole concentration, z the charge number, N Avogadro's number, z the charge number, q the electron charge, ζ the mobility, D the diffusivity, n the mole concentration of neutral species ($n_1 = n_{Li_2O}$, $n_2 = n_{Nb_2O_5}$), η the coefficient of ion generation and k the coefficient of ion recombination. Superscripts + and − indicate the cation and anion, respectively. When $\boldsymbol{b}$ is given, the equations are closed.

References

[1] D.C. Miller, T.L. Pernell, Fluid flow patterns in a simulated Garnet melt, J. Crystal Growth 57 (1982) 253–260.
[2] A.D.W. Jones, Spoke patterns, J. Crystal Growth 63 (1983) 70–76.
[3] D.T.J. Hurle, Convective transport in melt growth systems, J. Crystal Growth 65 (1983) 124–132.
[4] A.D.W. Jones, The stability of buoyancy-driven rolls aligned with a shear flow when the temperature gradient is nonlinear, Phys. Fluids 28 (1985) 31–36.
[5] K. Shigematsu, Y. Anzai, S. Morita, M. Yamada, H. Yokoyama, Growth conditions of subgrain-free $LiNbO_3$ single crystals by the Czochralski method, Jpn. J. Appl. Phys. 26 (1987) 1988–1996.
[6] Y. Miyazawa, S. Morita, H. Sekiwa, Effect of atmosphere gas on the convection in oxide melt, J. Jpn. Association Crystal Growth 19 (1) (1992) 14.
[7] S. Morita, H. Sekiwa, Y. Miyazawa, The growth of Al_2O_3 single crystal by Cz method (part II), J. Jpn. Association Crystal Growth 19 (1) (1992) 69.
[8] S. Morita, H. Sekima, H. Toshima, Y. Miyazawa, The growth of Al_2O_3 single crystals by the Czochralski method, J. Ceramic Society Japan 101 (1993) 108–112.
[9] K.W. Yi, K. Kakimoto, M. Eguchi, M. Watanabe, T. Shyo, T. Hibiya, Spoke patterns on molten silicon in Czochralski system, J. Crystal Growth 144 (1994) 20–28.
[10] C.J. Jing, N. Imaishi, Y. Yasuhiro, Y. Miyazawa, Three-dimensional numerical simulation of spoke pattern in oxide melt, J. Crystal Growth 200 (1999) 204–212.
[11] Y. Miyazawa, S. Morita, H. Sekiwa, Flow in oxide melt under magnetic field, J. Jpn. Association Crystal Growth 20 (2) (1993) 8.
[12] Y. Miyazawa, S. Morita, H. Sekiwa, Flow in oxide melt under magnetic field, J. Jpn. Association Crystal Growth 21 (3) (1994) 145.
[13] Y. Miyazawa, The flow in oxide melt under magnetic field, J. Jpn. Association Crystal Growth 22 (3) (1995) 23.
[14] Y. Miyazawa, T. Michino, The growth of TiO_2 single

crystals by the MCZ method, J. Jpn. Association Crystal Growth 23 (3) (1996) 74.
[15] Y. Miyazawa, T. Michino, Flow in GGG melts in a high magnetic field, J. Jpn. Association Crystal Growth 24 (2) (1997) 6.
[16] Y. Miyazawa, S. Morita, H. Sekiwa, Flow in oxide melts in a high magnetic field, J. Crystal Growth 166 (1996) 286–290.
[17] H. Minamikawa, Y. Miyazawa, Flow in oxide glass melts in high magnetic field, J. Jpn. Association Crystal Growth 25 (3) (1998) 80.
[18] Y. Miyazawa, H. Minamikawa, Flow in $YAlO_3$ melts in high magnetic field, J. Jpn. Association Crystal Growth 25 (3) (1998) 81.
[19] S. Uda, W.A. Tiller, The dissociation and ionization of $LiNbO_3$ melts, J. Crystal Growth 121 (1992) 155–190.
[20] D.T.J. Hurle, in: Handbook of Crystal Growth, vol. 2, Elsevier, Amsterdam, 1994 (Chapter 5).
[21] W.E. Langlois, K.M. Kim, J.S. Walker, Hydro-magnetic flows and effects on Czochralski silicon crystals, J. Crystal Growth 126 (1993) 352–372.
[22] H. Ozoe, K. Okada, The effect of the direction of the external magnetic field on the three-dimensional natural convection in a cubical enclosure, Int. J. Heat Mass Transfer 32 (10) (1989) 1939–1954.
[23] H. Ozoe, M. Iwamoto, Combined effects of crucible rotation and horizontal magnetic field on dopant concentration in a Czochralski melt, J. Crystal Growth 142 (1994) 236–244.
[24] L.A. Gorbunov, Effect of thermoelectromagnetic convection on the production of bulk single-crystals consisting of semiconductor melts in a constant magnetic field, Magnetohydrodynamics 23 (1987) 404–408.
[25] Yu.M. Gelfgat, L.A. Gorbunov, An additional source of forced convection in semiconductor melts during single-crystal growth in magnetic fields, Soviet Physics Dokl. 34 (1988) 470–473.
[26] J.J. Derby, L.J. Atherton, P.M. Gresho, An integrated process model for the growth of oxide crystals by the Czochralski method, J. Crystal Growth 97 (1989) 792–826.
[27] T. Tsukada, M. Hozawa, N. Imaishi, Global analysis of heat transfer in Cz crystal growth of oxide, J. Chem. Eng. Japan 27 (1994) 25–31.
[28] Y. Miyazawa, Private communication.
[29] T. Michino, Research Report, Namiki Seimitsu Houseki Co., Ltd., 1995.